Lithos 278-281 (2017) 215–228

Contents lists available at ScienceDirect

Lithos

journal homepage: www.elsevier.com/locate/lithos

Continental crust formation: Numerical modelling of chemical evolution and geological implications

U. Walzer*, R. Hendel

Institut f. Geowissenschaften, F.-Schiller-Universität, Jena 07743, Germany

ARTICLE INFO

Article history:
Received 11 August 2016
Accepted 14 December 2016
Available online 2 February 2017

Keywords:
Chemical differentiation
Continental crust
Episodicity
Surface heat flow
Thermoconvective mantle evolution
Water-dependent peridotite solidus

ABSTRACT

Oceanic plateaus develop by decompression melting of mantle plumes and have contributed to the growth of the continental crust throughout Earth's evolution. Occasional large-scale partial melting events of parts of the asthenosphere during the Archean produced large domains of precursor crustal material. The fractionation of arc-related crust during the Proterozoic and Phanerozoic contributed to the growth of continental crust. However, it remains unclear whether the continents or their precursors formed during episodic events or whether the gaps in zircon age records are a function of varying preservation potential. This study demonstrates that the formation of the continental crust was intrinsically tied to the thermoconvective evolution of the Earth's mantle. Our numerical solutions for the full set of physical balance equations of convection in a spherical shell mantle, combined with simplified equations of chemical continent–mantle differentiation, demonstrate that the actual rate of continental growth is not uniform through time. The kinetic energy of solid-state mantle creep (*Ekin*) slowly decreases with superposed episodic but not periodic maxima. In addition, laterally averaged surface heat flow (*qob*) behaves similarly but shows peaks that lag by 15–30 Ma compared with the *Ekin* peaks. Peak values of continental growth are delayed by 75–100 Ma relative to the *qob* maxima. The calculated present-day *qob* and total continental mass values agree well with observed values. Each episode of continental growth is separated from the next by an interval of quiescence that is not the result of variations in mantle creep velocity but instead reflects the fact that the peridotite solidus is not only a function of pressure but also of local water abundance. A period of differentiation results in a reduction in regional water concentrations, thereby increasing the temperature of the peridotite solidus and the regional viscosity of the mantle. By plausibly varying the parameters in our model, we were able to reproduce the intervals of the observed frequency peaks of zircon age determinations without essentially changing any of the other results. The results yield a calculated integrated continental growth curve that resembles the curves of GLAM, Begg et al. (2009), Belousova et al. (2010), and Dhuime et al. (2012), although our curve is less smooth and contains distinct variations that are not evident in these other curves.

1. Introduction

1.1. Integration of continental crust generation into a model of the thermochemical evolution of Earth

Early research suggested that Archean continental crustal material (e.g., tonalites and trondhjemites) was generated by the melting of mid-oceanic ridge basalt (MORB) slabs and Archean mantle wedges, with Proterozoic and Phanerozoic continental growth dominated by andesites and subduction-related rocks (Taylor and McLennan, 1995). Taylor and McLennan (1995) correctly recognised that the presence of abundant free water on Earth is one of the essential conditions for the generation of continental crustal material. However, recent basalt melting experiments indicate that modern MORB is not a plausible source for Archean continental crustal material that is dominated by tonalites, trondhjemites, and granodiorites (i.e., TTGs). The generation of TTGs requires a large ion lithophile element (LILE; i.e., K, Rb, Sr, Cs, Ba, and Eu^{2+} (Chauvel and Rudnick, 2016)) enriched source that is similar to the source of oceanic plateau basalts (Martin et al., 2014). The fact that water is not enriched at the base of present-day oceanic plateaus and that TTGs are produced by deep partial melting of hydrous basalt within the garnet stability field led Martin et al. (2014) to conclude that the occasional subduction of oceanic plateaus generated precursors to Archean continental crust. The present-day life expectancy of MORB crust is 150–200 Ma, whereas more buoyant oceanic plateaus are more likely to resist subduction. The upper layers of these plateaus are likely to peel off and be accreted to fertile continental margins or island arcs (Kerr, 2014).

* Corresponding author.
E-mail address: u.walzer@uni-jena.de (U. Walzer).

http://dx.doi.org/10.1016/j.lithos.2016.12.014
0024-4937/

The source region of an oceanic plateau must be hotter than the surrounding upper mantle (Kerr and Mahoney, 2007). The present-day mantle temperature beneath oceanic ridges is lower than the temperature of the mantle source of oceanic island basalts (OIB) (Herzberg et al., 2007; Lee et al., 2009). The modelling presented here indicates that elevated temperatures are the main driver of the partial melting of the source regions for oceanic plateau basalts. Lateral temperature gradients during the Phanerozoic have essentially been produced by large mantle plumes (McKenzie and Bickle, 1988) that arise as a consequence of the high temperature at the core–mantle boundary (CMB) (Davies, 2005). However, the volumetrically averaged Archean mantle temperature of our model is about 210 K higher than the present-day temperature of the mantle, a difference that is both consistent with komatiite research and suggests that some other process caused the elevated temperature of these mantle sources during the Archean, a process that was subsequently subdued during the Proterozoic and Phanerozoic.

van Kranendonk et al. (2011) and Brown (2014) used geological observations to suggest that one-sided subduction and steady-state plate tectonics initiated at about 3.0 Ga. This assumption is based mainly on the observation that prior to 3.0 Ga the subcontinental lithospheric mantle (SCLM) contained only peridotitic inclusions whereas later SCLM material preserved in diamonds contained eclogitic mineral inclusions. However, the modelling presented in this study does not impose any such restrictions, primarily as there are a number of different proposals for the timing of the onset of present-day type of subduction (cf. Fig. B11, where B refers to Appendix B). The possibility of a lack of modern-style oceanic crustal subduction in the Eoarchean and Mesoarchean also means that attempting to explain the early chemical evolution of the continental crust and the residual mantle by the differentiation of the oceanic crust is impossible, consistent with the geochemical reasoning of Martin et al. (2014). In addition, we know that 50%–70% of the continental crustal mass had formed by the beginning of the Neoarchean (Taylor and McLennan, 2009), with Belousova et al. (2010) concluding that more than 60% of the existing continental mass was generated before 2.5 Ga. This strongly suggests that the Eoarchean and Mesoarchean evolution of the Earth determined the initial conditions for the processes that operated during the Neoarchean, Proterozoic, and Phanerozoic, rather than the opposite. This in turn indicates that models of the geochemical evolution of the mantle that involve the early development of oceanic crustal subduction with later incorporation of chemical continental differentiation are erroneous. This conclusion is independent of the fact that continental differentiation must have involved two or more steps. Therefore, any modelling of the evolution of the continental crust and mantle must incorporate the notion that an essential part of the continental crust evolved prior to the onset of present-day steep subduction of the oceanic crust. In addition, crust–mantle differentiation is intrinsically tied to the thermal evolution of the mantle, indicating the importance of integrating a simplified model of continental–crust differentiation and accretion into a three-dimensional (3D) spherical-shell model of the chemical and thermal evolution of the Earth. This type of model contrasts with many other similar models in that it more closely accounts for the geological and mineralogical history of the Earth.

1.2. Are rates of continental crustal growth uniform through time?

The temporal distribution of zircon U–Pb ages throughout Earth history has peaks and troughs that can be explained by two end-member hypotheses, as follows.

(1) Zircon age peaks represent episodes of enhanced continental crustal generation with increased magmatism occurring prior to the collision of newly generated continental segments with older continents (Arndt and Davaille, 2013; Rino et al., 2004; Walzer and Hendel, 2013; Yin et al., 2012).

(2) Zircon age peaks are artefacts that reflect variations in preservation potential, as outlined by Hawkesworth et al. (2009), who stated that the time intervals preceding supercontinent formation have moderate preservation potential, whereas periods of supercontinent amalgamation have the highest preservation potential. This led Spencer et al. (2015) to emphasise that continental collision isolates collision-related tectonomagmatic belts from various tectonic processes, a process that increases the longevity of detrital zircon isotopic signatures. This type of magmatism is thought to be continuous and non-episodic. Zircon preservation potential is also thought to be low during supercontinent break-up, with Cawood et al. (2013) suggesting that continental growth occurred by a continuous rather than episodic process, consistent with research by Belousova et al. (2010) and Dhuime et al. (2012), who concluded that the rate of continental growth is relatively uniform through time.

Recent research supports hypothesis (1) and it is probably uncontested that the majority of continental growth during the Phanerozoic and presumably also the Proterozoic occurred in oceanic and continental arc settings. This view is supported by multi-element (Ba to Yb) variation diagrams (Niu et al., 2013) that show the similar compositions of bulk continental crust (Rudnick and Gao, 2003) and island-arc basalts (Elliott, 2003). In addition, water is necessary for the generation of granitoid magmas. One of the main regions for the generation of hydrous magmas at the base of the crust is island arc settings, where water is added to the mantle wedge from the downgoing slab. In contrast, the base of present-day oceanic plateaus is anhydrous (Arndt, 2013). The largest Phanerozoic magmatic arcs were generated above subduction zones where 50% of the magmatism was derived from the mantle wedge, with the remaining 50% derived from recycled upper-plate crustal material (Ducea et al., 2015). In addition, Paterson and Ducea (2015) described episodic arc magmatism where flare-ups produce 100–1000 times more magmatic mass that is added to continental arcs compared with periodic lulls in magmatism. These Phanerozoic peaks in magma addition rates do not coincide with supercontinent formation but are consistent with peaks in the zircon age record (Ducea et al., 2015).

Given the above, the second main aim of our modelling is to determine whether continent generation is a continuous or episodic process. The modelling should be based on a physically sound and complete system of equations and should be able to predict other observable variables such as laterally averaged heat flow and the present-day volume of continental crust.

1.3. Origin of juvenile contributions to the continental crust

Present day plume-generated hotspots are anomalous volcanic regions that are not associated with contemporaneous plate boundaries (Davies et al., 2015). Current magmatism is the result of two different processes, namely plumes and plate tectonics, both of which are likely to have existed in the past. If modern plate tectonics with oceanic crustal subduction, arc formation, and accretion only initiated after 3.0 Ga then it is likely that continental crustal material that formed before this time evolved from oceanic plateau material. Early research suggested that the SCLM developed by the stacking of material derived from subducted oceanic slabs, although it is perhaps more likely that the Eoarchean and Mesoarchean SCLM and associated continental crustal material are the residues of very high-degree partial melting of the ambient upper mantle (a process that no longer occurs) or mantle plume material (Griffin et al., 2013). Similarly, Arndt et al. (2009) suggested that the main source

of forsterite-rich olivine and magnesian orthopyroxene within the early SCLM is the residue of high-degree partial melting of the mantle that occurred in unusually hot mantle plume heads. We do not explicitly presuppose these findings but our dynamical model is likely to be compatible with them.

2. Model description

2.1. Continent–mantle differentiation

Kerr and Mahoney (2007) and Kerr (2014) state that oceanic plateaus form from mantle plumes generated by decompression melting and are derived from peridotitic source regions with higher potential temperatures than the surrounding ambient mantle. These source regions also contain elevated concentrations of incompatible elements and water, although the latter would have been reduced as a result of any continent–mantle differentiation events. Our model also uses formulae that ensure that decreasing water abundances increase the temperature of the peridotite solidus in the source region after differentiation. Kerr (2014) reported that oceanic plateaus are more buoyant than normal oceanic crust. This means that the upper layers of such plateaus can be peeled off and accreted to existing continents. We incorporated this mechanism in condensed form into the Terra code that is based on a full system of physical balance equations. Our model also incorporates the temporal changes that have occurred in continental crustal generation and accretion processes during the evolution of the Earth. The fact that our model is global means that we incorporated the simple common accretion mechanism of Walzer and Hendel (2008) (Appendix A). This accretion is followed by movement of tracers that represent continental crustal material with a common angular velocity vector ($\vec{\omega}$) that is a function of time (t). This assumption is based on the devolatilisation of the SCLM, meaning that post-accretion continental tracers move like a raft driven by bulk convection and by contact with oceanic lithospheric plates, with these tracers free to be carried by oceanic plates prior to accretion. It is not our intention to model a special accreted orogen in distinct steps, although this is possible using two-dimensional models. Instead, we present a 4.5 Ga 3D model of the entire evolution of the mantle after the majority of the mantle became solid, meaning in turn that we can determine solid-state creep. We assume that instantaneous differentiation only occurs in particular volumes associated with partial melting, a process that generates individual geochemical reservoirs (cf. Table 1). Molten and low-density material is also instantaneously moved to the surface layer. Our model also incorporates geochemical observations, especially an improved theory of geochemical reservoirs (Stracke, 2012; Stracke et al., 2005; Willbold and Stracke, 2006) that are not necessarily spatially separated but are characterised by tracers that are entrained by solid-state creep. Only continental tracers are forced to move near the surface until they collide with an older continent, causing accretion. Melting is defined via a water-abundance-dependent solidus (cf. Table B1), with convection driven mainly by primordial heat and heating as a result of the distributions of U, Th, and K, whose abundances are redistributed by differentiation, entrainment by convection, and horizontal movement of the continents. This means that the continental tracers only carry heat-producing elements and water. A description of the Terra code used during this study is presented in Walzer and Hendel (2008). Here, we use input parameters that vary as a function of depth (h), namely the Grüneisen parameters, the peridotite solidus (which also varies as a function of water abundance), the viscosity of solid-state creep, thermal expansivity, specific heat (c_p; cf. Table B1 in Appendix B), and improved numerical simulations. Other input parameters used in the modelling are given in Table B4.

Table 1
$a_{\mu\prime}$ abundances of heat-producing elements (U, Th, and K). Bulk Silicate Earth (BSE): ON&Pal (O'Neill and Palme, 2008) represent a cosmochemical estimate. Two geochemical estimates, based on chondritic compositions, are given by Arev (Arevalo et al., 2009) and McC&B (McCulloch and Bennett, 1994). The parameterised thermal evolution models are represented by Schu (Schubert et al., 2001). Depleted Mantle (DM): Sa&Str (Salters and Stracke, 2004), McC&B (see above), and Ar&McD (Arevalo and McDonough, 2010). Continental Crust (CC): Rud&Gao (Rudnick and Gao, 2003), McC&B (see above). Oceanic Crust (OcCr): W&K (White and Klein, 2013), Plank (Plank, 2013), McC&B (see above); inc. sed. = includes sediments.

Reservoir	**BSE**			
Reference	ON&Pal	Arev	McC&B	Schu
Index			(1)	
$a_{\mu\prime}$(U)	10 ppb	20 ± 4 ppb	20.3 ppb	35 ± 4 ppb
$a_{\mu\prime}$(Th)	40 ppb	80 ± 13 ppb	85.3 ppb	140 ± 14 ppb
$a_{\mu\prime}$(K)	140 ppm	280 ± 60 ppm	250 ppm	350 ± 35 ppm
Reservoir	**DM**			
Reference	Sa&Str	McC&B	Ar&McD	
Index		(4)		
$a_{\mu\prime}$(U)	4.7 ± 1.4 ppb	6.6 ppb	8 ± 2 ppb	
$a_{\mu\prime}$(Th)	13.7 ± 4.1 ppb	17.0 ppb	22 ± 4 ppb	
$a_{\mu\prime}$(K)	60 ± 17 ppm	110 ppm	152 ± 30 ppm	
Reservoir	**CC** (incl. sed.)	**CC**	**OcCr** (incl. sed.)	**OcCr**
Reference	Rud&Gao	McC&B	W&K,Plank	McC&B
Index		(3)		(2)
$a_{\mu\prime}$(U)	1.47 ± 0.25 ppm	0.94 ppm	0.15 ± 0.02 ppm	0.047 ppm
$a_{\mu\prime}$(Th)	6.33 ± 0.50 ppm	4.70 ppm	0.58 ± 0.07 ppm	0.12 ppm
$a_{\mu\prime}$(K)	1.63 ± 0.12 wt%	0.946 wt%	0.16 ± 0.02 wt%	0.06 wt%

2.2. Mantle radioactivity and generalised mantle reservoirs

This section discusses the abundances of heat-producing elements used in our model. Primordial heat and mantle radioactivity provide the power for mantle convection, continent–mantle differentiation, and the majority of the tectonic processes that occur on Earth. However, estimates of mantle radiogenic heat generation vary by a factor of more than 20 (Šrámek et al., 2013). As such, we undertook a geochemical investigation prior to modelling (Appendix C) and considered building our convection–differentiation system on a non-chondritic Earth model. The abundances of U, Th, and K within the competing geochemical models are given in Table 1, and evolutionary computations using the Terra code indicated that a non-chondritic model (e.g., O'Neill and Palme, 2008) yielded unrealistic and very low laterally averaged heat flow values (*qob*) as well as inconsistencies of a different nature (cf. Appendix C, especially the last paragraph). However, use of the U, Th, and K abundances proposed by Schubert et al. (2001), which are based on a parameterised geodynamic evolution model, yields clearly excessive *qob* values. This led us to use the models of Arevalo et al. (2009) and McCulloch and Bennett (1994), especially as these models lie between the compositions of the non-chondritic and parameterised models. This, combined with the fact that the values of McCulloch and Bennett (1994) are within the error limits stated by Arevalo et al. (2009) and to ensure that our modelling is comparable with the results of Walzer and Hendel (2008), led us to exclusively use the elemental abundances of McCulloch and Bennett (1994).

The depletion of parts of the mantle is intimately linked to the production of continental crustal material, as demonstrated by a first-order observation diagram (Fig. 5.1) of White (2015), where a

multi-element (from Cs to Lu) variation diagram shows variations in the average composition of MORB, the depleted mantle (DM) (Salters and Stracke, 2004; Workman and Hart, 2005), and the continental crust (Rudnick and Gao, 2014; Taylor and McLennan, 1995; Wedepohl, 1995), normalised to the bulk silicate Earth (BSE) composition of McDonough and Sun (1995). The DM and continental crustal compositions have inversely correlating peaks and troughs, suggesting that the former complements the latter. Any deviations from this complementarity suggest the presence of minor mantle reservoirs. The andesitic composition of the average continental crust also requires the additional removal of parts of the lower continental crust (LCC) by foundering and (for ages younger than about 3.0 Ga) by slab-associated erosion of the LCC. The melting of DM material also generates oceanic crust that rarely contributes to continental growth. Our modelling approximates these reservoirs using tracers that are entrained by solid-state flow and can be mixed as well as differentiated, with the latter especially true of regions undergoing partial melting. The time-dependent U, Th, and K abundances in a given grid cell are also the result of the weighted averaging of the U, Th, and K abundances of these tracers.

Our modelling uses the concept of chemical mantle "reservoirs" as expressed by Stracke et al. (2005) and Willbold and Stracke (2006). Here, this concept is used as a tool to describe the rather inhomogeneous nature of the Earth's mantle. We compute the average abundance of each heat-producing element in each grid cell at each point in time t using the chemical reservoir tracers of the immediate neighbourhood (cf. Table 1). The evolution of heat production density is defined by a numerical solution derived from the full set of physical balance equations (cf. Appendix A) in the spherical shell that represents the mantle, as well as chemical differentiation equations. In general, there are no sharp boundaries between different mantle reservoirs (cf. Fig. B6) barring the two types of lower lithospheric boundary. The mantle is essentially heated from within by the heat production density (Q), determined as follows:

$$Q = \rho \cdot \sum_{\nu=1}^{4} a_{\mu\nu} a_{if\nu} H_{0\nu} \cdot e^{-t/\tau_\nu} \tag{1}$$

where ρ denotes density, ν the sequential number of the heat-producing isotope, $a_{\mu\nu}$ the abundances of the four reservoirs of McCulloch and Bennett (1994) outlined in Table 1, $a_{if\nu}$ the isotope abundance factor, $H_{o\nu}$ the specific heat production of the νth radionuclide at 4567.6 Ma, and τ_ν is the decay time or the $1/e$ lifetime. We solve the full set of conservation equations of mass, momentum, and energy plus the continent–mantle differentiation equations during our modelling, with radioactive atoms redistributed by chemical differentiation according to the equations presented in Appendix A of Walzer and Hendel (2008). The evolution of the heat production density (Q) is incorporated into the energy balance (i.e., in Eq. (A.28)), yielding an immediate feedback between chemical continent–mantle differentiation and mantle convection. The spherical shell of our present model has free-slip and impermeable boundary conditions for both the Earth's surface and the CMB. We start at an age of $\tau = 4490$ Ma, with the assumed initial condition of the mantle being the equality of the initial and solidus temperatures (cf. Table B1 and Eq. (2)), and a zero creeping velocity. The upper surface is isothermal at 288 K, with application of the cooling core–mantle evolution model of Steinbach et al. (1993) enabling adjustment of the CMB temperature (T_c) after each time step according to the heat flow through the CMB. We assume that a homogeneous core is in thermodynamic equilibrium, following Steinbach and Yuen (1994) and Honda and Iwase (1996). The quantity T_c is a constant as a function of the *location* within the entirety of the CMB surface. This is necessary because of the low viscosity of the outer core (OC) and the presence of hydromagnetic convection within the OC. The *temporal* T_c decrease is not prescribed but is a result of the dynamics of the system, thus also including cooling of the Earth's core. As a result, there is a slight additional heating of the mantle from below.

2.3. Dependence of the mantle solidus on water abundance, mantle viscosity and other input parameters, and balance equations

Taylor and McLennan (2009) emphasised that planetary evolution, like planetary formation, is dominated by stochastic and unpredictable events. This may be the case for the accretion of the Earth, although we hypothesise that the thermal and chemical evolution of the Earth after the initial distribution of chemical elements and isotopic mixtures within the earliest solid-state mantle should be predictable and calculable. Clearly there are also stochastic features in the "fluid" dynamics of solid-state convection (Walzer and Hendel, 2009, 2013), although Taylor and McLennan (2009) suggested that water content is not only responsible (1) for the subduction of oceanic lithospheric plates but also (2) for the generation of continents. The problem of self-consistent generation of oceanic lithospheric plates has been treated by Trompert and Hansen (1998), Moresi and Solomatov (1998), Bercovici (1998), Tackley (2000a,b), Richards et al. (2001) and Walzer et al. (2004). Dymkova and Gerya (2013) presented a 2D numerical model that demonstrates that intra-oceanic subduction can start spontaneously when porous fluid is present within the oceanic crust and along plate boundaries. The present-day hydrosphere represents only 0.0226% (1.35×10^{21} kg) of the Earth's mass (5.98×10^{24} kg) (cf. e.g. Gargaud et al., 2012). The *solubility* of water in the mantle is relatively high but is dependent on depth within the mantle (Mierdel et al., 2007), reaching a minimum within the present-day asthenosphere. There exists 100 ppm H_2O or 150 ± 50 ppm H_2O in the global DM (Dixon et al., 2002; Salters and Stracke, 2004), with Dixon et al. (2002) suggesting that recycled eclogitised oceanic crust (HIMU) contains about 600 ppm H_2O and the focal-zone reservoir (FOZO) about 750 ppm H_2O. These studies indicate that the high $^3He/^4He$ ratio of the FOZO rules out its generation by the mixing of DM and HIMU material. However, this view remains contentious because Gonnermann and Mukhopadhyay (2009) suggested that high ^3He abundances, high $^3He/^4He$ ratios and high ^{40}Ar abundances can be retained during recycling. In addition, Bolfan-Casanova (2005) indicated that solubility of water within perovskite of the lower mantle is controversial because it is difficult to produce samples free of impurities. Litasov et al. (2003) reported that (Al,Fe)-perovskites dissolve up to 1800 ppm H_2O whereas the MORB system can contain up to 110 ppm H_2O, and Marty (2012) suggested that the bulk Earth contains 2700 ± 1350 ppm H_2O, within a range of 1000 to 3000 ppm H_2O considering uncertainties and the results of other authors. Finally, Hirschmann (2006) estimated that the mantle source for OIB contains 300 to 1000 ppm H_2O. Here, we follow Litasov (2011) and use the conventional value of 1000 ppm H_2O for the McCulloch and Bennett (1994) BSE component of Table 1. It should also be noted that our simplified convection–differentiation system means that only U, Th, K, and H_2O need to be considered.

Our model uses the T_{m0}, T_{m5}, and T_{m10} values in Table B1 and Fig. B1 within Appendix B to define the solidus of the mantle peridotite, with upper mantle values from Litasov (2011). Lower mantle solidus curves were extrapolated using

$$\frac{1}{T_{sol}} \cdot \frac{dT_{sol}}{dP} = \frac{2}{K}\left(\gamma_{ax} - \frac{1}{3}\right) \tag{2}$$

where T_{sol} is the solidus, P is pressure, and K is the bulk modulus according to PREM (Preliminary reference Earth model; cf. Dziewonski and Anderson, 1981). The flow of water is only partly modelled and we only assume that each particular differentiation

event has a solidus $T_{m10}(r)$ that is replaced by $T_{m0}(r)$ in the differentiation region (cf. Table B1.). The new values of this physical property then move with convective flow and recovery is only possible by mixing with fertile regions of the mantle. This process was modelled using a tracer approach following Walzer and Hendel (2008). We determine γ_{ax} as a Grüneisen parameter using the acoustic gamma as follows:

$$\gamma_a = \frac{1}{6}\frac{K_T}{K_S+(4/3)\mu}\left[\left(\frac{\partial K_S}{\partial P}\right)_T+\frac{4}{3}\left(\frac{\partial \mu}{\partial P}\right)_T\right] + \frac{1}{3}\frac{K_T}{\mu}\left(\frac{\partial \mu}{\partial P}\right)_T-\frac{1}{6} \quad (3)$$

for depths between 771 and 2741 km. It is remarkable that γ_a can be completely determined from geophysically observable variables obtained from PREM. This means that our model is independent of specific chemical or mineralogical models at these depths. The model of Walzer and Hendel (2008) employs the Vashchenko–Zubarev gamma, although the modelling of the present study includes all of the available information on shear modes. The seismic shear modulus is denoted by μ, with the associated pressure derivative denoted by $d\mu/dP$ and temperature by T. The quantities K_S and K_T signify the adiabatic and isothermal bulk moduli, respectively. It would also be simple to apply Eq. (3) to other parts of the mantle, although Stacey and Davis (2009) reported that seismological estimates of dK/dP and $d\mu/dP$ within the upper mantle, crust, and the D″ layer generate physically implausible depth variations of the Grüneisen parameter γ. As such, we use the gamma estimates of Stacey and Davis (2009), γ_{SD}, for the depth range h < 771 km and for the D″ layer; otherwise, our model uses γ_a. We call this combination the extended acoustic gamma, γ_{ax}. The modelling shown in Fig. B2 indicates that the γ_{ax} curve for the lower mantle is appropriately located between the somewhat larger values of γ_{SD} and the somewhat smaller values of the Debye gamma, γ_D, which was calculated as follows:

$$\gamma_D = \frac{1}{3}-\frac{1}{3}\left[d\ln\left(\frac{1}{v_p^3}+\frac{2}{v_s^3}\right)/d\ln\rho\right] \quad (4)$$

where v_p and v_s indicate the seismic compressional and shear wave velocities, respectively. These velocities and the density, ρ, were taken from PREM. Computing mantle dynamics requires γ_{ax} values that are determined directly from observable quantities. This meant that the energy balance Eq. (A.28) was transformed to ensure one summand is explicitly dependent on γ_{ax} and another contains the deviatoric stress tensor τ_{ik} that is linearly dependent on shear viscosity η (cf. Eq. (A.29)). The viscosity in turn is nonlinearly dependent on the melting temperature (T_m; cf. Eq. (5)), with the latter being dependent on γ_{ax}:

$$\eta(r,\theta,\phi,t) = 10^{r_n}\cdot\frac{\exp(c\,\overline{T_m/T_{av}})}{\exp(c\,\overline{T_m/T_{st}})}\cdot\eta_4(r) \cdot\exp\left[c_t\cdot T_m\left(\frac{1}{T}-\frac{1}{T_{av}}\right)\right] \quad (5)$$

where r is the radius, θ the colatitude, ϕ the longitude, t is time, r_n is the viscosity level parameter, T_{av} is the laterally averaged temperature, T_{st} is the initial temperature profile, and T is the temperature as a function of r, θ, ϕ, and t. To consider $MgSiO_3$ perovskite, $c = 14$ should be used, whereas considering MgO wüstite should use $c = 10$ according to Yamazaki and Karato (2001). This means that the lower mantle value of c should lie between 10 and 14. However, for numerical reasons we can only use $c = 7$. For the lateral-variability term we use $c_t = 1$. The quantity r_n serves to systematically vary the convective vigour from run to run, meaning that even unrealistic cases were investigated in this study. The quantity $\eta_4(r)$ is a newly derived viscosity profile for the initial temperature and for $r_n = 0$. The profile $\eta_4(r)$ differs from the $\eta_3(r)$ term used by Walzer and Hendel (2008). Our viscosity function η_4 is compared with the viscosity profile of Mitrovica and Forte (2004) in Fig. B8, with the present-day laterally averaged shear viscosity of run 498 compared with the viscosity of Mitrovica and Forte (2004) in Fig. B9. To ensure our computations are verifiable and are usable by the scientific community, we have provided a list of γ_{ax}, γ_D, γ_{SD}, $T_{m0}(K)$, $T_{m5}(K)$, $T_{m10}(K)$, $\log\eta_4(Pa\cdot s)$, $T_{ad}(K)$, $\alpha(10^{-6}\cdot K^{-1})$, and $c_p(J/(kg\cdot K))$ values as a function of depth, h (km), in Table B1 within Appendix B. The quantities T_{m0}, T_{m5}, and T_{m10} represent different water-concentration-dependent peridotite solidi that are explained in the caption of Fig. B1, with T_{ad} representing the adiabatic mantle temperature, α representing thermal expansivity, and c_p representing specific heat at constant pressure. The α/c_p ratio was calculated using PREM, as follows:

$$\alpha/c_p = (\gamma_{ax}\cdot\rho)/K_T \quad (6)$$

$$\text{where} \quad K_T = (1+\alpha\cdot\gamma_{ax}\cdot T)^{-1}\cdot K_s \quad (7)$$

The other important differential equation is the momentum balance equation (Eq. (A.31)), which also contains τ_{ik} and therefore η, T_m, and γ_{ax}. We solved the full set of equations during this study, with the conservation of mass, momentum, energy, (implicitly) angular momentum, and the four sums of the number of atoms of the pairs $^{238}U-^{206}Pb$, $^{235}U-^{207}Pb$, $^{232}Th-^{208}Pb$, and $^{40}K-^{40}Ar$ being guaranteed by these equations (cf. Appendix A of this paper and appendix A of Walzer and Hendel (2008)). Recent research by an international group (cf. the Acknowledgments section of this paper) has considerably improved the Terra code that was originally written by Baumgardner (1983, 1985). A compilation of the numerical improvements is given in Section 2.2 of Walzer et al. (2013), with all the hitherto discussed physical quantities serving as input parameters and Eq. (A.30) serving as an equation of state. This means that density (ρ) varies not only as a function of temperature (T) and pressure (P) but also as a function of the two mineral phase transitions at depths of about 410 and 660 km, meaning that the influence of any deflection of these phase boundaries is expressed by the Clausius–Clapeyron slope. The melting temperature (T_m) also influences the conditions of chemical differentiation, with major volume partial melting only occurring if

$$T > f_3\cdot T_m \quad (8)$$

is fulfilled or when the water abundance exceeds water solubility (Litasov, 2011; Mierdel et al., 2007), where f_3 is somewhat smaller than or equal to 1. We varied f_3 in the different Terra runs and assume that if Eq. (8) is fulfilled, not only are the incompatible elements redistributed according to Table 1 but also a high percentage of water leaves the peridotite within the volume being considered. This escape generates an increase of T_m according to Fig. B1 or Table B1. The solidus considered in our models is not only a function of pressure but also of water abundance and therefore also of time (t). The modelled continents are generated according to the algorithm in Appendix A of Walzer and Hendel (2008). The occurrence of ultrahigh-pressure metamorphism indicates that macroscopic and deep continental subduction is possible after $\tau = 3.0$ Ga (Komiya, 2011; Massonne, 2013; Schertl and O'Brien, 2013). We also agree with Stracke's (2012) statement that the subduction of oceanic plates, of certain amounts of lower continental crust, and of small parts of the upper continental crust is an important process that causes mantle enrichment. The

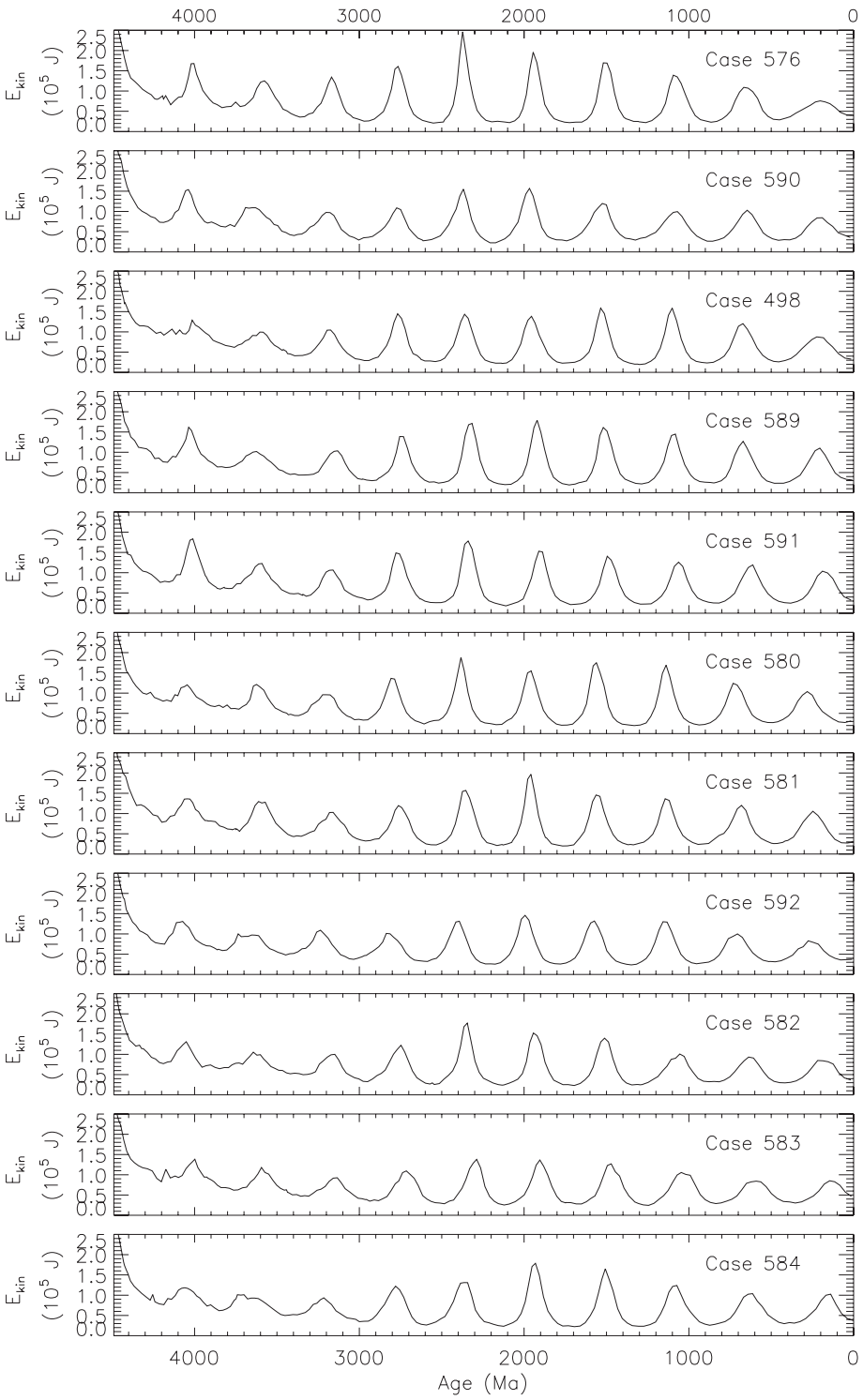

Fig. 1. Kinetic energy of mantle convection as a function of age. We varied the melting criterion parameter f_3 from 0.999 (top panel) to 0.979 (bottom panel) in steps of 0.002. This modelling used constant values of $r_n = 0.5$, $\sigma_y = 120$ MPa, and $k = 5.0$ W/(m • K).

formation of new continental crustal material in our model causes it to be entrained by the corresponding oceanic lithospheric plate. If this new continental crustal material comes into contact with pre-existing continental crustal material, the former will accrete to the latter. This accretion process is the only supplementary assumption that we have added to the equation system described above. Oceanic lithospheric plates self-consistently develop at the surface of our spherical shell model because the uppermost 285 km of the mantle and the crust in our model have an effective viscosity (η_{eff}) that is implemented as follows:

$$\eta_{eff} = \min\left[\eta(P,T), \frac{\sigma_y}{2\dot{\varepsilon}}\right] \tag{9}$$

where σ_y is a viscoplastic yield stress and $\dot{\varepsilon}$ denotes the second invariant of the strain-rate tensor. The quantity σ_y is a constant

for a given run but this variable was varied from case to case. It is impossible to generate plates with a purely viscous constitutive equation (Moresi and Solomatov, 1998), and the existence of an asthenosphere appears to be an additional requirement for the production of oceanic plates. The asthenosphere was numerically described by $\eta_4(r)$ as specified in Table B1 and was computed using Eq. (5). Yoneda et al. (2009) measured a thermal conductivity (k) of 5.00 W/(m · K) for perovskite, although we varied the thermal conductivity of the mantle between runs, with the best results obtained using $k = 5.00$ W/(m · K). It is important to note that our model can include both stable continents *and* plate tectonics, similar to the models of Lenardic et al. (2004), O'Neill et al. (2008), Yoshida and Santosh (2011), Rolf et al. (2012), and Yoshida (2012). We also emphasise that our model continents were not artificially imposed on the convection model.

3. Results and discussion

Our modelling used the Terra code to repeatedly solve the convection–segregation equations (cf. Appendix A of this paper and

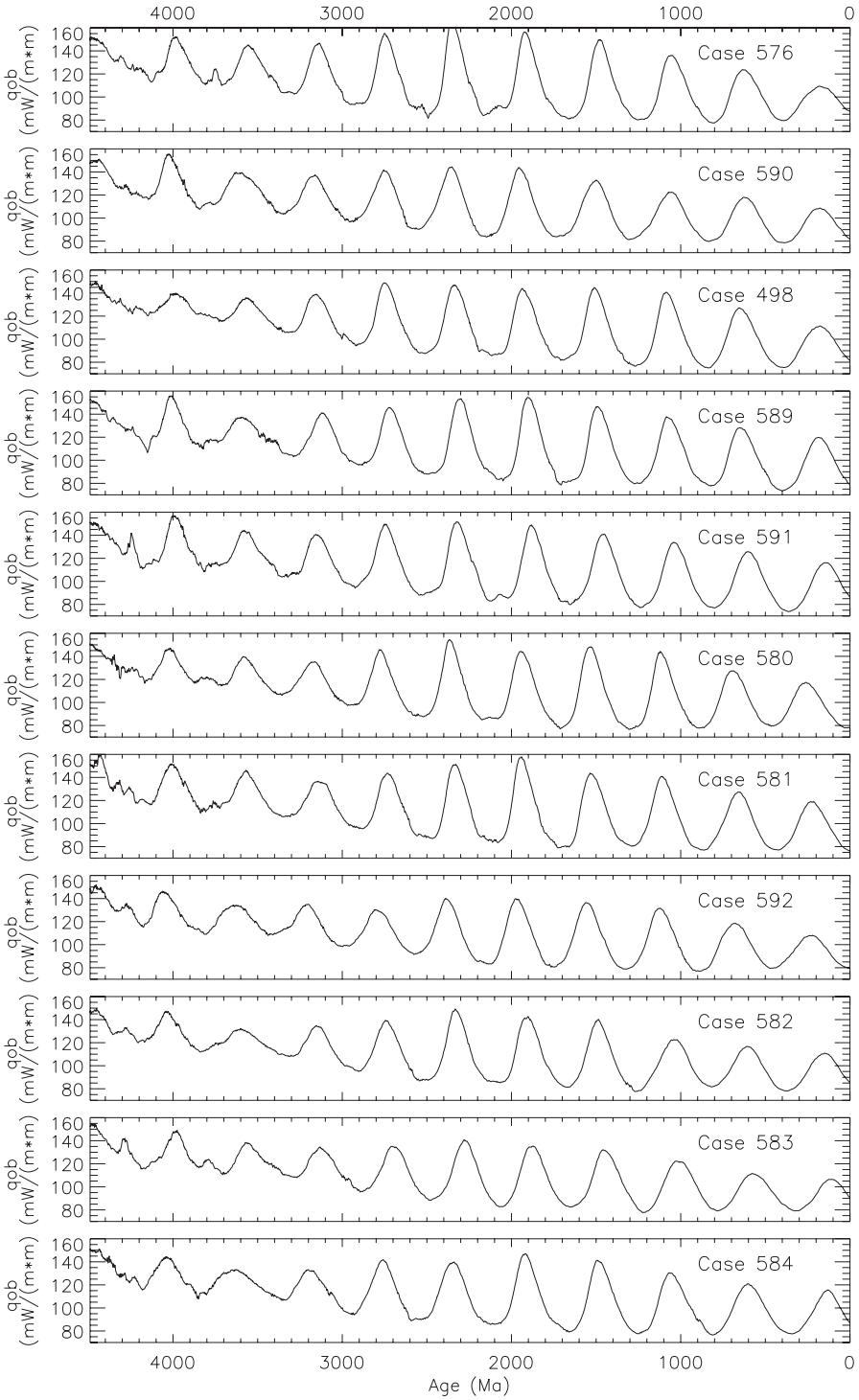

Fig. 2. Laterally averaged surface heat flow as a function of age, showing the same runs as in Fig. 1.

appendix A of Walzer and Hendel, 2008) for the last 4490 Ma of the Earth's evolution. The fields of the velocity vector $v_i(r,\theta,\phi,t)$ of solid-state creep, of temperature $T(r,\theta,\phi,t)$, and of the percentage distribution of chemical reservoirs (cf. Table 1) as a function of (r,θ,ϕ,t) were obtained for each time step. This modelling also yielded a number of realistic solutions for a moderate range of neighbouring input values. However, for reasons of brevity we have confined ourselves to several highlights. All of our modelling yielded episodic continental growth. We systematically varied the viscosity-level parameter (r_n; cf. Eq. (5)), viscoplastic yield stress (σ_y; cf. Eq. (9)), thermal conductivity (k; cf. Eq. (A.28)), and the melting-criterion parameter (f_3; cf. Eq. (8)) from run to run. At first, we used r_n values between 0.2 and 0.8 and σ_y values between 100 and 140 MPa. Thereby we used constant values of $k = 5.00$ W/(m · K) and $f_3 = 0.995$. We investigated the difference (d_c^*) between the computed and observed percentages of continental crust at the present-day Earth's surface. This comparison used a value of 40.35% of the Earth's surface that is covered by present-time continents. The boundary between continents and

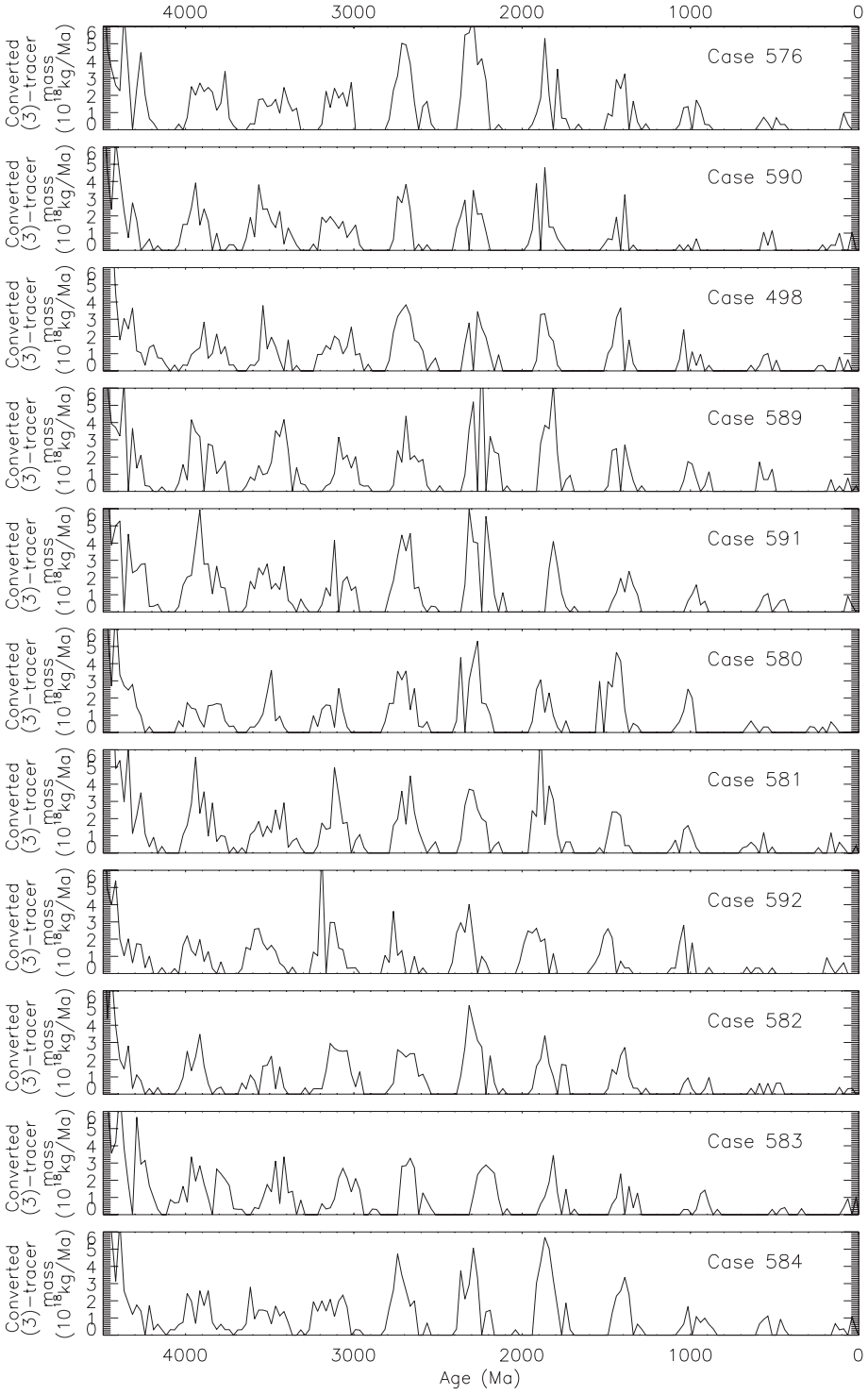

Fig. 3. Episodes of juvenile magmatic activity that contributed to continental growth as a function of age, showing the same runs as in Fig. 1.

oceans is defined by the minimum of the hypsometric curve situated between the continental and the oceanic peak. Very small d_c^* values (i.e., good agreements between observation and computation) were obtained for models using r_n values from just below 0.5 to 0.6. However, d_c^* values appear to be only slightly dependent on variations in σ_y values. The best numerical agreement was obtained for values of $r_n = 0.5$ and $\sigma_y = 120$ MPa. In addition, decreasing d_c^* *any* values converge to the corresponding observed quantities (cf. Fig. B4 or the corresponding plot for run 498). The next stage of modelling used constant values of $r_n = 0.5$ and $\sigma_y = 120$ MPa, and we varied f_3 values between 0.9 and 1.0, and k values between 3.8 and 5.3 W/(m · K). Plotting the theoretical present-day continental surface (p_c) in percent values in a f_3–k plot yields a correlation where k increases with f_3 if only the best solutions are considered. This indicates a trade-off between k and f_3. However, when considering all other quantities such as laterally averaged surface heat flow (*qob*) in the corresponding f_3–k diagrams, only runs with thermal conductivity values around $k = 5.0$ W/(m · K) yield realistic solutions. This is consistent with the independent findings of Yoneda et al. (2009) and the assumption outlined by Monnereau and Yuen (2010).

Keeping $r_n = 0.5$, $\sigma_y = 120$ MPa, and $k = 5.0$ W/(m · K) constant in Figs. 1 to 3 yields a temporally averaged Rayleigh number $Ra \approx 10^8$. The foundation of our viscosity distribution is shown in Eq.(5), where the viscosity function η_4 is listed in Table B1 (eighth column). Fig. B8 compares our viscosity function η_4 with the viscosity profile of Mitrovica and Forte (2004). Cserepes et al. (2000) also proposed a similar viscosity distribution with high mid-mantle values and a significant influence of the transition layer. The cooling of the Earth causes an increase in viscosity; Fig. B9 shows the present-day laterally averaged viscosity profile. However, the Rayleigh number at 4000 Ma was 5.59 times larger than the present-day value. Compared with viscosity, thermal conductivity (k) has only a minor influence on the thermal and chemical evolution of the Earth, as seen in the comparative runs. As such, we kept this value constant during individual runs but varied it from case to case.

Fig. 1 shows that convective activity (more precisely the kinetic energy or E_{kin} of solid-state convection) generally decreases as a function of time but not as rapidly and continuously as predicted by models of parameterised convection. In contrast to these simple models, our modelling also yields periods of time with elevated activity that are *not* strictly periodically distributed. These episodes of augmented convective activity dynamically evolve from our system of equations without any further assumptions. Fig. 1 shows that varying f_3 values yields times of maximum convective activity that are highly correlated. In addition, the input parameters used in the cases shown in Fig. 2 are entirely comparable to those used in the cases shown in Fig. 1.

Fig. 2 shows the evolution of the laterally averaged surface heat flow (*qob*) according to our model with f_3 varying from panel to panel. Fig. 2 also shows that decreasing *qob* values are superposed by episodes of elevated heat flow. However, *qob* maxima occur somewhat *after* the corresponding E_{kin}-maxima, indicating the presence of a time lag as a result of the time needed for convection to carry the heat from the interior of the mantle to the surface. Denoting the age by τ yields a time lag Δ_ν^+ for an individual peak ν as follows:

$$\Delta_\nu^+ = \tau\,[Max_\nu(E_{kin})] - \tau\,[Max_\nu(qob)] = \tau_\nu^+ - \tau_\nu \qquad (10)$$

where the superscript $^+$ refers to the $E_{kin}(\tau)$ curve and the plain τ_ν is the age of the corresponding *qob* maximum. Labrosse and Jaupart (2007) presented a semi-empirical evolution model that modified the conventional heat budget equation of parameterised models and revealed that the laterally averaged heat flow, *qob*, fluctuates with a difference of 400 Ma between neighbouring peaks. Our dynamic model also shows fluctuations in *qob* with nearly sinusoidal components, with an average temporal distance of 429 Ma for the last seven *qob* maxima (e.g., case 498 shown in Fig. 2). The other cases shown in Fig. 2 yield similar values.

Pollack et al. (1993) used a dataset of 24,774 observations to determine a present-day total surface heat flow of $q_{tot} = 44.2 \pm 1$ TW, corresponding to $qob = 86.7 \pm 2.0$mW/m^2. Jaupart et al. (2007) re-evaluated the same dataset and obtained a value of $q_{tot} = 46 \pm 3$ TW, corresponding to $qob = 90.2 \pm 5.9$mW/m^2. Davies and Davies (2010) revised the estimate of the Earth's total surface heat flow using 38,347 measurements, with separate averages for different geologic domains, yielding a value of 47 ± 2 TW that corresponds to $qob = 92.1 \pm 3.9$mW/m^2. Fig. 2 shows that our 3D dynamic evolution model yields laterally averaged heat flow values (*qob*) that are a function of age, with *qob* values decreasing as a function of time but less quickly than is suggested by parameterised thermal evolution models and with a sinusoidal component superimposed. This result, combined with the uncertainties in the initial conditions of these models, suggests that it is better not to compare present-day *qob* values, but to compare qob_9 values (i.e., the temporal average of *qob* over the last 900 Ma) with observational values. The qob_9 values obtained from our runs (cf. Table B2, second column) agree well with $qob = 92.1 \pm 3.9$mW/m^2, an instantaneous value that fits well into the range of *qob* values for the last 900 Ma. The mechanism outlined in appendix A by Walzer and Hendel (2008) suggest that chemical continent–mantle differentiation yields considerably larger stochastic contributions than variations in $E_{kin}(t)$ and $qob(t)$ values. This expectation is corroborated by Fig. 3, where juvenile continental mass is plotted as a function of age with f_3 values varying from panel to panel. This figure indicates that continental crustal growth is episodic, with each episode separated from the next by a period of quiescence that increases in duration toward the Phanerozoic (Fig. 3). The clarity of these inactive periods increases after the introduction of the water-dependent peridotite solidus (cf. Fig. B1) into our models. Magmatically active time-spans are characterised by the loss of a significant amount of water, which means T nearly reaches T_m values. This in turn causes an exhaustion, where T_{sol} transiently increases to a higher curve as a result of devolatilisation. Moyen and Martin (2012) and other researchers have used geologic observations to suggest that continental growth was indeed episodic. The zircon- and sandstone-based age data of Condie and Aster (2010) and Bradley (2011) yield peaks of magmatic activity at 2697, 1824, *1435*, 1047, 594, *432*, and *174* Ma, which are reproduced by run 498 (cf. Fig. 3, third panel). This also indicates that it is possible to reproduce not only the essential features of the episodicity of continental growth but also some of the processes that cause this episodicity and the temporal links between this episodicity and zircon age data. However, this finding does not exclude the possibility of preservation potential playing a role. Fig. 3 is consistent with Arndt and Davaille's (2013) statement that zircon ages are not uniformly distributed and that peaks are separated by longer periods in which zircon ages are rare or absent.

The next point to consider is the water dependence of the peridotite solidus. Fig. B5 (panel B) shows a case *without* a water-dependent peridotite solidus but with the same number of grid points and the same number of chemical tracers representing U, Th, and K abundances and at cooler starting conditions. This modelling again yields an episodic temporal distribution of the juvenile contribution to the total mass of continental crust but without any significant quiescence between episodes. Our modelling *with* water-dependent peridotite solidus values (cf. Fig. 3) suggests that considerably more time is needed to fill the exhausted region with fertile mantle material again than is the case for models without a water-dependent peridotite solidus. We also checked the resolution of this model by performing each run twice with different amounts of the tracers that represent the abundances of U, Th, and K, all of which are

relevant for internal heating within these models. Basic runs (B-runs) used about 10.5×10^6 tracers with comparative runs (C-runs) using 84×10^6 tracers. Comparing panels B and C in Fig. B5 indicates that both basic and comparative runs have similar temporal evolutions despite the presence of stochastic effects.

Walzer and Hendel (2008) and papers cited therein made specific assumptions regarding the continents based on observations. These include South America moving westward despite the eastward-dipping subduction of the Nazca Plate. There is no further slab that could drive the South American continent in a westward direction. The India–Asia collision occurred after 66 Ma but before 58 Ma (Hu et al., 2016), with Aitchison et al. (2007) concluding that India collided into Asia at 35 Ma and with India also continuing to move northward after this collision. Archean and early Proterozoic parts of the continental crust are also underlain by very thick SCLM that is nearly the same age as the overlying continental crust. There is no asthenosphere under the old eastern and central parts of Australia. All of this suggests that the movement of the continental crust is driven by bulk convection whereas slab pull is the dominant driving force for the movement of purely oceanic plates. Of course, interactions occur between these two processes. In addition, Stracke (2012) used geochemical arguments to conclude that only a minor part of the upper continental crust has been subducted into the mantle; consequently, we self-consistently model the growth of continents, but after crust formation the red markers that delineate the continental crust move like rafts on the mantle. Tracers of geochemical reservoirs (cf. Table 1) are freely mixed in the rest of the mantle by convection that is computed by solving all relevant balance equations. The result is a marble cake mantle (e.g., Fig. B6) where (yellow) depleted regions of the mantle slightly dominate the upper mantle, especially in areas beneath the lithosphere. Our modelling did not reproduce any present-day *chemical* layering within the mantle.

In comparison to the maxima of the $qob(\tau)$ curves of Fig. 2, the episodes of the continent-mantle differentiation of Fig. 3 occur somewhat later. This temporal delay was systematically investigated by replacing continental growth clusters by bell-shaped curves using a least-squares method, with the maxima of both the bell-shaped curves and the $qob(\tau)$ value used to determine the lag.

$$\Delta_\nu = \tau[Max_\nu(qob)] - \tau[Max_\nu(bellcurve)] = \tau_\nu - \tau_\nu^* \tag{11}$$

The largest age differences occur between mantle convection kinetic energy maxima and the bell-curve maxima of the crust–mantle differentiation curve:

$$\Delta_\nu^\times = \tau[Max_\nu(E_{kin})] - \tau[Max_\nu(bellcurve)] = \tau_\nu^+ - \tau_\nu^* \tag{12}$$

The mean values averaged over the last seven temporal differences of the maxima Δ_ν^+, Δ_ν, and $\Delta_\nu^\times$ are designated by an additional subscript $_M$ that is used in the legend of Figs. 4 (b), (c), and 5(b–d). Fig. 4 (a) shows the combinations of r_n and σ_y values that yield computed continental crustal areas that approximate present-day continental crustal areas. As such, we used fixed values of $r_n = 0.5$ and $\sigma_y = 120$ MPa for investigations based on the k–f_3 diagram. Fig. 4 (b) indicates that the time lag between the surface heat flow maxima and corresponding crust–mantle differentiation maxima ranges between 50 and 75 Ma if we only consider runs that are favourable in all respects. This result, combined with the data shown in Fig. 4 (c), shows that realistic runs yield temporal lags between the maximum intensity of mantle convection and the corresponding maximum of crust–mantle differentiation that range between 80 and 100 Ma. The temperature (T) that is volumetrically averaged over the whole mantle plus crust is here termed T_{mean}, with the average of this value over the last 900 Ma designated T_{mean9}. Cases with $k = 5.0$ W/(m · K) and $0.98 \leq f_3 \leq 1.0$ yield T_{mean9} values that realistically lie between 2340 K and

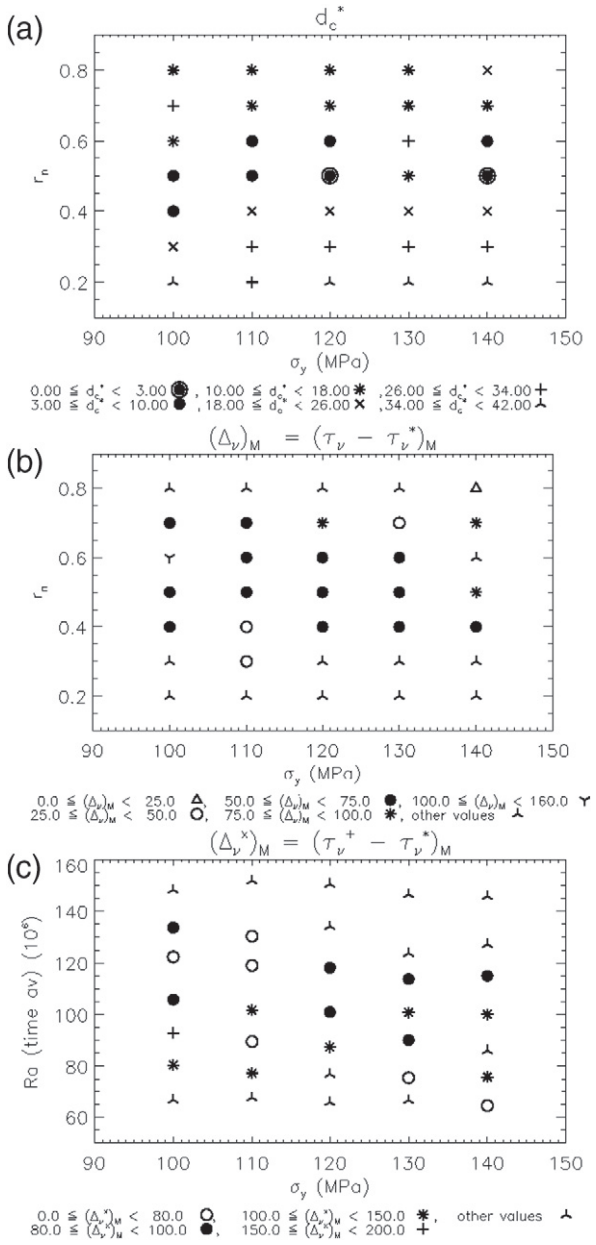

Fig. 4. (a) σ_y–r_n plot of the distribution of the absolute value of the difference (d_c^*) between the percentage of computed and observed present-day (40.35%) continental Earth's surface. (b) Mean value of the temporal difference Δ_ν (cf. Eq. (11)), here termed $(\Delta_\nu)_M$, plotted in a σ_y–r_n diagram. (c) Mean temporal difference $\Delta_\nu^\times$ (cf. Eq. (12)), herein called $(\Delta_\nu^\times)_M$, plotted in a σ_y – *Ra* diagram, where *Ra* is the temporally averaged Rayleigh number. The numerical values in the legends for (b) and (c) are expressed in Ma.

2360 K. This narrow f_3–k area also yields qob_9 values between 92.0 and 97.5 mW/m^2 (Fig. 5). This is similar to the results presented by Davies and Davies (2010) and as such this interval is considered to be realistic. Fig. 5 (b) to (d) shows $(\Delta_\nu)_M$,$(\Delta_\nu^\times)_M$, and $(\Delta_\nu^+)_M$ values in f_3–k diagrams (cf. Eqs. (11), (12), and (10), respectively), yielding realistic time delay values for $k = 5.0$ W/(m · K) and $0.985 \leq f_3 \leq 0.995$. Fig. 6 shows the present-day distribution of continents and oceans with a computed continental crustal surface cover of 42.2% of the Earth's surface, slightly higher than the observed value of 40.35%.

Irreversible processes such as radioactive decay mean that E_{kin} (Fig. 1) and qob (Fig. 2) values generally decline. However, this

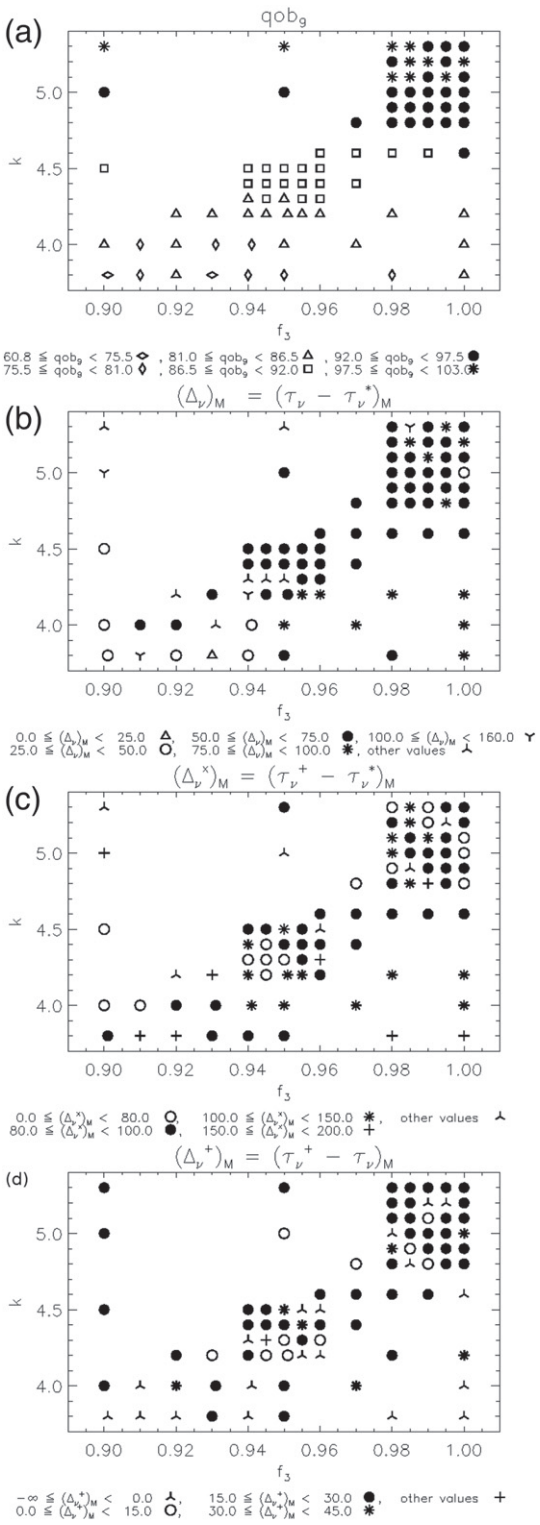

Fig. 5. Diagrams showing relevant parameters plotted in f_3-k space, where f_3 is the melting criterion parameter and k is thermal conductivity expressed as W/(m • K). (a) Symbols represent the laterally averaged heat flow that was additionally time-averaged over the last 900 Ma (qob_9; expressed in mW/m^2). (b) Symbols designate classes of mean values of temporal differences between maxima of the laterally averaged surface heat flow (qob) and maxima of magmatic activity; cf. Eq. (11). Numbers in the legend are in Ma. (c) Symbols represent classes of mean values of temporal differences (in Ma) between the maximum intensities of convective flow and the subsequent magmatic intensity maximum; cf. Eq. (12). (d) Symbols describe classes of mean temporal difference values (in Ma) between convective intensity maxima and subsequent surface heat flow maxima; cf. Eq. (10).

decay is superposed by slow and nearly sinusoidal variations that can be explained as follows. The ringwoodite–perovskite-plus-magnesiowüstite phase transition and the high-viscosity transition layer (Fig. B8) act as an obstacle that sometimes causes nearly separate bulk convection circulations in the upper and lower mantle. These periods are characterised by a special profile of laterally averaged temperature (Fig. B7), although this barrier is occasionally removed, causing a period of whole-mantle bulk convection that results in high surface heat flow and a loss of the pronounced temperature maximum below the 660 km discontinuity. However, the subduction of oceanic plates has only operated since around 3.0 Ga. The high seismicity near slabs at the depth of the transition layer is also influenced by the high viscosity of this region. Our modelling needs to distinguish between bulk convection, convection due to downgoing slabs of oceanic lithosphere, and convection driven by mantle plumes. Bulk convection has always operated, as the movement of continents containing deep SCLM material was driven by bulk convection long before slab-driven convection began to operate. The physical derivation of the high-viscosity transition layer may also require the discrimination of water solubility and water abundance. Mierdel et al. (2007) reported a possible procedure to do this.

In contrast to other evolution models, we do not prescribe the number, size, form, or distribution of the evolving continents but instead develop these in a self-consistent manner. As in our forerunner model (Walzer and Hendel, 2008, e.g. Fig. 11), we found that the computed continents resemble the observed distribution of the continental crust.

Finally, the bulk convection in our models includes periods where this is divided into upper and lower mantle convection. However, this *convective* layering becomes unstable at times, causing an increase in the kinetic energy within these flows (Fig. 1). There is a time lag that delays the arrival of this hot material at or near the surface and the generation of an associated augmented laterally averaged surface heat flow (Fig. 2). The presence of fertile and water-rich peridotitic material beneath the lithosphere would also mean that these elevated temperatures would lead to chemical differentiation. Walzer and Hendel (2008) produced computational oceanic plates in a forerunner of the present model where the introduction of a viscoplastic yield stress σ_y was essential to this process. The oceanic lithosphere carries the U-, Th-, and K-enriched upper differentiation product until it encounters a continental margin. Here, we accrete this material to the continent. This is an artificial feature of the model but it is realistic. In addition, the fact that this transport of enriched material (e.g., oceanic plateaus and, additionally, arcs in later geological eras) takes some time before it is accreted means that the peaks of the episodes of juvenile magmatic activity (Fig. 3) have different timings to the corresponding heat flow maxima. Davies (1995) has already published a 2D model with a phase transformation barrier that leads to episodic mantle overturns. This model also proposed a connection between these events and episodes of crust formation.

4. Conclusions

The model of crust–mantle evolution presented in this study leads to the following conclusions.

The actual rate of continental growth is **not** uniform through time. A contrary conclusion is improbable from a physical point of view.

Our model not only solves one particular problem but leads to a better comprehension of a range of geological and geophysical observations, strengthening its conclusiveness (cf. Figs. 3, 4, 5, 6, B11, B3, B2, B6, B7, and B10; Tables B2 and B3, and further items within this section),

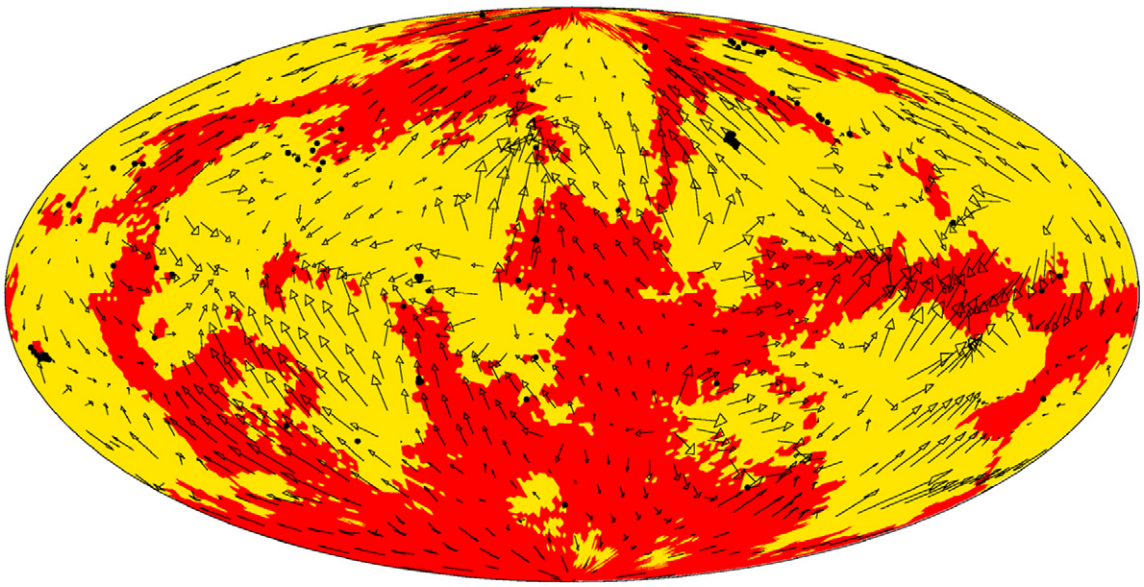

Fig. 6. A representative present-day distribution of the continental crust (red), the oceanic crust (yellow), and oceanic plateaus (black dots) in run 498, with $r_n = 0.5$, and $\sigma_y = 120$ MPa. This model yields computed continents that cover 42.2% of the Earth's surface. Arrows signify present-day surface creep velocities.

Running the Terra code with variable viscoplastic yield stress (σ_y) and viscosity-level parameter (r_n; cf. Eq. (5)) values from case to case yields a connected Ra-σ_y domain with a minimum difference between theoretical and observed present-day percentages of continental crust at the Earth's surface. The quantity r_n is a measure of the time-averaged Rayleigh number, Ra, and neighbouring runs in the above-mentioned Ra–σ_y domain (e.g. case 498; cf. Fig. 3) show the smallest deviation from observed data.

We also varied heat conductivity (k) and melting-criterion parameter (f_3) values, with the best results obtained for $k = 5.0$ W/(m · K), $\sigma_y = 120$ MPa, and $r_n = 0.5$, with the latter value corresponding to $Ra \approx 10^8$.

The kinetic energy of solid-state creep (E_{kin}) of the Earth's mantle decreases slowly over time, with this decrease being superposed by clearly separated maxima that have similar but not uniform temporal spacings.

The temporal evolution of the laterally averaged surface heat flow (qob) behaves similarly, although the $qob(t)$ maxima occur 15–30 Ma after E_{kin} maxima. We also obtain a bijective allocation between E_{kin} and qob maxima, with each case containing evidence of which elevated convective mantle movement event caused which individual surface heat flow peak.

Our model shows that the continental crust grows episodically between intervals of quiescence, with magmatically active time spans delayed by 75–100 Ma relative to qob-maxima, although their assignment to the preceding qob maximum event is unambiguous.

Our model results are consistent with the zircon age maxima of Condie and Aster (2010) at 2697, 1824, 1047, and 594 Ma, and with the ages of detrital zircons from sandstones and metasandstones (Fig. 16 of Bradley, 2011). The complete sequence of observed frequency peaks (at 2697, 1824, *1435*, 1047, 594, *432*, and *174* Ma) is remarkably well reproduced by our theoretical model curve of continental growth (Fig. 3, case 498, third panel).

Each episode of continental crustal generation is separated from the next by a period of quiescence. This is caused mainly by the novel computational feature of making the peridotite solidus not only a function of pressure but also of water abundance and therefore of time.

The physical mechanisms that underlie the above results are discussed in the second part of Section 3.

The magnitude of the computed volumetrically averaged temperature drop (ΔT_{mean}) is about 210 K, a value that agrees well with the observed temperature decrease derived from komatiite research (cf. Chapter B2).

Our computed qob_9 values match the observed values of $qob = 92.1 \pm 3.9 \mathrm{mW/m^2}$ reported by Davies and Davies (2010).

Our calculated integrated continental growth curve also agrees well the curves of GLAM, Begg et al. (2009), Belousova et al. (2010), and Dhuime et al. (2012), although our curve is less smooth (cf. Fig. B11).

Acknowledgments

We thank J. Baumgardner (inventor of the code Terra), H.-P. Bunge, P. Bollada, S. Brune, H. Davies, R. Davies, C. Köstler, M. Mohr, M. Müller, and J. Weismüller, among others within the group of Terra developers, for stimulating discussions. We also thank Dave Stegman for providing us with his particle code. This paper benefited from geochemical and geological discussions with L. Viereck, C. Heubeck, J. Kley, and K. Ustaszewski. We thank the Editor (A. C. Kerr) and two anonymous reviewers for constructive comments that improved the clarity of the paper, and the Steinbuch Center for Computing, Karlsruhe, for providing computational time as part of grant *sphshell*.

Appendix A. Supplementary data

Supplementary information to this article (Appendix A: Balance equations; Appendix B: Supplementary sections and data; Appendix C: Geochemical considerations regarding the assumed abundances of U, Th, and K in the mantle) can be found online at http://dx.doi.org/10.1016/j.lithos.2016.12.014.

References

Aitchison, J.C., Ali, J.R., Davis, A.M., 2007. When and where did India and Asia collide? Journal of Geophysical Research: Solid Earth 112 (B5).

Arevalo, R., McDonough, W.F., 2010. Chemical variations and regional diversity observed in MORB. Chemical Geology 271 (1), 70–85.

Arevalo, R., McDonough, W.F., Luong, M., 2009. The K/U ratio of the silicate Earth: insights into mantle composition, structure and thermal evolution. Earth and Planetary Science Letters 278 (3), 361–369.

Arndt, N., Coltice, N., Helmstaedt, H., Gregoire, M., 2009. Origin of Archean subcontinental lithospheric mantle: some petrological constraints. Lithos 109 (1), 61–71.

Arndt, N., Davaille, A., 2013. Episodic Earth evolution. Tectonophysics 609, 661–674.

Arndt, N.T., 2013. The formation and evolution of the continental crust. Geochemical Perspectives 2 (3), 405–528.

Baumgardner, J.R., 1983. A Three-dimensional Finite Element Model for Mantle Convection. Ph.D. thesis. Univ. of California, Los Angeles.

Baumgardner, J.R., 1985. Three-dimensional treatment of convective flow in the Earth's mantle. Journal of Statistical Physics 39 (5-6), 501–511.

Begg, G., Griffin, W., Natapov, L., O'Reilly, S.Y., Grand, S., O'Neill, C., Hronsky, J., Djomani, Y.P., Swain, C., Deen, T., et al. 2009. The lithospheric architecture of Africa: seismic tomography, mantle petrology, and tectonic evolution. Geosphere 5 (1), 23–50.

Belousova, E.A., Kostitsyn, Y.A., Griffin, W.L., Begg, G.C., O'Reilly, S.Y., Pearson, N.J., 2010. The growth of the continental crust: constraints from zircon Hf-isotope data. Lithos 119, 457–466.

Bercovici, D., 1998. Generation of plate tectonics from lithosphere-mantle flow and void-volatile self-lubrication. Earth and Planetary Science Letters 154, 139–151.

Bolfan-Casanova, N., 2005. Water in the Earth's mantle. Mineralogical Magazine 69 (3), 229–257.

Bradley, D., 2011. Secular trends in the geologic record and the supercontinent cycle. Earth Science Reviews 108, 16–33.

Brown, M., 2014. The contribution of metamorphic petrology to understanding lithosphere evolution and geodynamics. Geoscience Frontiers 5 (4), 553–569.

Cawood, P.A., Hawkesworth, C., Dhuime, B., 2013. The continental record and the generation of continental crust. Geological Society of America Bulletin 125 (1-2), 14–32.

Chauvel, C., Rudnick, R.L., 2016. Large-ion lithophile elements. In: White, W. (Ed.), Encyclopedia of Geochemistry. Springer International Publishing, Switzerland, pp. 1–3.

Condie, K.C., Aster, R.C., 2010. Episodic zircon age spectra of orogenic granitoids: the supercontinent connection and continental growth. Precambrian Research 180, 227–236.

Cserepes, L., Yuen, D.A., Schroeder, B.A., 2000. Effect of the mid-mantle viscosity and phase-transition structure on 3D mantle convection. Physics of the Earth and Planetary Interiors 118 (1), 135–148.

Davies, D.R., Rawlinson, N., Iaffaldano, G., Campbell, I.H., 2015. Lithospheric controls on magma composition along Earth's longest continental hotspot track. Nature 525 (7570), 511–514.

Davies, G.F., 1995. Punctuated tectonic evolution of the Earth. Earth and Planetary Science Letters 136 (3), 363–379.

Davies, G.F., 2005. A case for mantle plumes. Chinese Science Bulletin 50 (15), 1541–1554.

Davies, J.H., Davies, D.R., 2010. Earth's surface heat flux. Solid Earth 1, 5–24.

Dhuime, B., Hawkesworth, C.J., Cawood, P.A., Storey, C.D., 2012. A change in the geodynamics of continental growth 3 billion years ago. Science 335 (6074), 1334–1336.

Dixon, J.E., Leist, L., Langmuir, C., Schilling, J.G., 2002. Recycled dehydrated lithosphere observed in plume-influenced mid-ocean-ridge basalt. Nature 420 (6914), 385–389.

Ducea, M.N., Paterson, S.R., DeCelles, P.G., 2015. High-volume magmatic events in subduction systems. Elements 11 (2), 99–104.

Dymkova, D., Gerya, T., 2013. Porous fluid flow enables oceanic subduction initiation on Earth. Geophysical Research Letters 40 (21), 5671–5676.

Dziewonski, A.M., Anderson, D.L., 1981. Preliminary reference Earth model. Physics of the Earth and Planetary Interiors 25, 297–356.

Elliott, T., 2003. Tracers of the slab. In: Eiler, J. (Ed.), Inside the Subduction Factory. American Geophysical Union, Washington, pp. 23–45.

Gargaud, M., Martin, H., López-García, P., Montmerle, T., Pascal, R., 2012. Young Sun, Early Earth and the Origins of Life: Lessons for Astrobiology. Springer, Berlin.

Gonnermann, H.M., Mukhopadhyay, S., 2009. Preserving noble gases in a convecting mantle. Nature 459 (7246), 560–563.

Griffin, W., Begg, G., O'Reilly, S.Y., 2013. Continental-root control on the genesis of magmatic ore deposits. Nature Geoscience 6 (11), 905–910.

Hawkesworth, C.J., Cawood, P.A., Kemp, A.I.S., Storey, C.D., Dhuime, B., 2009. A matter of preservation. Science 323, 49–50.

Herzberg, C., Asimow, P.D., Arndt, N., Niu, Y., Lesher, C., Fitton, J., Cheadle, M., Saunders, A., 2007. Temperatures in ambient mantle and plumes: constraints from basalts, picrites, and komatiites. Geochemistry, Geophysics, Geosystems 8 (2). Q02006.

Hirschmann, M.M., 2006. Water, melting, and the deep Earth H_2O cycle. Annual Review of Earth and Planetary Sciences 34, 629–653.

Honda, S., Iwase, Y., 1996. Comparison of the dynamic and parameterized models of mantle convection including core cooling. Earth and Planetary Science Letters 139, 133–145.

Hu, X., Wang, J., BouDagher-Fadel, M., Garzanti, E., An, W., 2016. New insights into the timing of the India–Asia collision from the Paleogene Quxia and Jialazi formations of the Xigaze forearc basin, South Tibet. Gondwana Research 32, 76–92.

Jaupart, C., Labrosse, S., Mareschal, J.C., 2007. Temperatures, heat and energy in the mantle of the Earth. In: Bercovici, D. (Ed.), Treatise on Geophysics. Mantle Dynamics vol. 7. Elsevier, Amsterdam, pp. 253–303.

Kerr, A.C., 2014. Oceanic plateaus. In: Holland, H.C., Turekian, K. (Eds.), The Crust. Treatise on Geochemistry vol. 4. Elsevier, Amsterdam, pp. 631–667.

Kerr, A.C., Mahoney, J.J., 2007. Oceanic plateaus: problematic plumes, potential paradigms. Chemical Geology 241 (3), 332–353.

Komiya, T., 2011. Continental recycling and true continental growth. Russian Geology and Geophysics 52, 1516–1529.

Labrosse, S., Jaupart, C., 2007. Thermal evolution of the Earth: secular changes and fluctuations of plate characteristics. Earth and Planetary Science Letters 260 (3), 465–481.

Lee, C.T.A., Luffi, P., Plank, T., Dalton, H., Leeman, W.P., 2009. Constraints on the depths and temperatures of basaltic magma generation on Earth and other terrestrial planets using new thermobarometers for mafic magmas. Earth and Planetary Science Letters 279 (1), 20–33.

Lenardic, A., Nimmo, F., Moresi, L., 2004. Growth of the hemispheric dichotomy and the cessation of plate tectonics on Mars. Journal of Geophysical Research 109, E02003.

Litasov, K., Ohtani, E., Langenhorst, F., Yurimoto, H., Kubo, T., Kondo, T., 2003. Water solubility in Mg-perovskites and water storage capacity in the lower mantle. Earth and Planetary Science Letters 211 (1), 189–203.

Litasov, K.D., 2011. Physicochemical conditions for melting in the Earth's mantle containing a C-O-H fluid (from experimental data). Russian Geology and Geophysics 52, 475–492.

Martin, H., Moyen, J.F., Guitreau, M., Blichert-Toft, J., Le Pennec, J.L., 2014. Why Archaean TTG cannot be generated by MORB melting in subduction zones. Lithos 198-199, 1–13.

Marty, B., 2012. The origins and concentrations of water, carbon, nitrogen and noble gases on Earth. Earth and Planetary Science Letters 313-314, 56–66.

Massonne, H.J., 2013. Constructing the pressure-temperature path of ultrahigh-pressure rocks. Elements 9 (4), 267–272.

McCulloch, M.T., Bennett, V.C., 1994. Progressive growth of the Earth's continental crust and depleted mantle: geochemical constraints. Geochimica et Cosmochimica Acta 58 (21), 4717–4738.

McDonough, W.F., Sun, S.S., 1995. The composition of the Earth. Chemical Geology 120, 223–253.

McKenzie, D., Bickle, M., 1988. The volume and composition of melt generated by extension of the lithosphere. Journal of Petrology 29 (3), 625–679.

Mierdel, K., Keppler, H., Smyth, J.R., Langenhorst, F., 2007. Water solubility in aluminous orthopyroxene and the origin of the Earth's asthenosphere. Science 315, 364–368.

Mitrovica, J.X., Forte, A.M., 2004. A new inference of mantle viscosity based upon joint inversion of convection and glacial isostatic adjustment data. Earth and Planetary Science Letters 225 (1), 177–189.

Monnereau, M., Yuen, D.A., 2010. Seismic imaging of the D′′ and constraints on the core heat flux. Physics of the Earth and Planetary Interiors 180 (3), 258–270.

Moresi, L., Solomatov, V., 1998. Mantle convection with a brittle lithosphere: thoughts on the global tectonic styles of the Earth and Venus. Geophysical Journal International 133 (3), 669–682.

Moyen, J.F., Martin, H., 2012. Forty years of TTG research. Lithos 148, 312–336.

Niu, Y., Zhao, Z., Zhu, D.C., Mo, X., 2013. Continental collision zones are primary sites for net continental crust growth. A testable hypothesis. Earth-Science Reviews 127, 96–110.

O'Neill, C.J., Lenardic, A., Griffin, W.L., O'Reilly, S.Y., 2008. Dynamics of cratons in an evolving mantle. Lithos 102, 12–24.

O'Neill, H.S.C., Palme, H., 2008. Collisional erosion and the non-chondritic composition of the terrestrial planets. Philosophical Transactions of the Royal Society A: Mathematical, Physical and Engineering Sciences 366 (1883), 4205–4238.

Paterson, S.R., Ducea, M.N., 2015. Arc magmatic tempos: gathering the evidence. Elements 11 (2), 91–98.

Plank, T., 2013. The chemical composition of subducting sediments. In: Holland, H.D., Turekian, K.K. (Eds.), Treatise on Geochemistry. vol. 4. Elsevier, Oxford, pp. 607–629.

Pollack, H.N., Hurter, S.J., Johnson, J.R., 1993. Heat flow from the Earth's interior: analysis of the global data set. Reviews of Geophysics 31, 267–280.

Richards, M.A., Yang, W.S., Baumgardner, J.R., Bunge, H.P., 2001. Role of a low-viscosity zone in stabilizing plate tectonics: implications for comparative terrestrial planetology. Geochemistry, Geophysics Geosystems 2, 1026.

Rino, S., Komiya, T., Windley, B.F., Katayama, I., Motoki, A., Hirata, T., 2004. Major episodic increases of continental crustal growth determined from zircon ages of river sands; implications for mantle overturns in the Early Precambrian. Physics of the Earth and Planetary Interiors 146, 369–394.

Rolf, T., Coltice, N., Tackley, P., 2012. Linking continental drift, plate tectonics and the thermal state of the Earth's mantle. Earth and Planetary Science Letters 351, 134–146.

Rudnick, R.L., Gao, S., 2003. Composition of the continental crust. In: Rudnick, R. (Ed.), The Crust. Treatise on Geochemistry vol. 3. Elsevier, Amsterdam, pp. 1–64.

Rudnick, R.L., Gao, S., 2014. 4.1 - composition of the continental crust. In: Holland, H.D., Turekian, K.K. (Eds.), Treatise on Geochemistry. Elsevier, Oxford, pp. 1–51.

Salters, V.J.M., Stracke, A., 2004. Composition of the depleted mantle. Geochemistry, Geophysics Geosystems 5 (5, 27).

Schertl, H.P., O'Brien, P.J., 2013. Continental crust at mantle depths: key minerals and microstructures. Elements 9 (4), 261–266.

Schubert, G., Turcotte, D.L., Olson, T.R., 2001. Mantle Convection in the Earth and Planets. Cambridge University Press, Cambridge, UK.

Spencer, C.J., Cawood, P.A., Hawkesworth, C.J., Prave, A.R., Roberts, N.M., Horstwood, M.S., Whitehouse, M.J., et al. 2015. Generation and preservation of continental crust in the Grenville Orogeny. Geoscience Frontiers 6 (3), 357–372. http://dx.doi.org/10.1016/j.gsf.2015.12.001.

Šrámek, O., McDonough, W.F., Kite, E.S., Lekić, V., Dye, S.T., Zhong, S., 2013. Geophysical and geochemical constraints on geoneutrino fluxes from Earth's mantle. Earth and Planetary Science Letters 361, 356–366.

Stacey, F.D., Davis, P.M., 2009. Physics of the Earth. 4th edition, Cambridge University Press, Cambridge, UK.
Steinbach, V., Yuen, D.A., 1994. Effects of depth-dependent properties on thermal anomalies produced in flush instabilities from phase transitions. Physics of the Earth and Planetary Interiors 86, 165–183.
Steinbach, V., Yuen, D.A., Zhao, W.L., 1993. Instabilities from phase transitions and the timescales of mantle thermal convection. Geophysical Research Letters 20, 1119–1122.
Stracke, A., 2012. Earth's heterogeneous mantle: a product of convection-driven interaction between crust and mantle. Chemical Geology 330-331, 274–299.
Stracke, A., Hofmann, A.W., Hart, S.R., 2005. FOZO, HIMU and the rest of the mantle zoo. Geochemistry, Geophysics, Geosystems 6, Q05007.
Tackley, P.J., 2000a. Self-consistent generation of tectonic plates in time-dependent, three-dimensional mantle convection simulations. Part 1. Pseudoplastic yielding. Geochemistry, Geophysics, Geosystems 1, 2000GC000036.
Tackley, P.J., 2000b. Self-consistent generation of tectonic plates in time-dependent, three-dimensional mantle convection simulations. Part 2. Strain weakening and asthenosphere. Geochemistry, Geophysics, Geosystems 1, 2000GC000043.
Taylor, S.R., McLennan, S.M., 1995. The geochemical evolution of the continental crust. Reviews of Geophysics 33, 241–265.
Taylor, S.R., McLennan, S.M., 2009. Planetary Crusts: Their Composition, Origin and Evolution. Cambridge University Press, Cambridge, UK.
Trompert, R., Hansen, U., 1998. Mantle convection simulations with rheologies that generate plate-like behavior. Nature 395, 686–689.
van Kranendonk, M.J., et al. 2011. Onset of plate tectonics. Science 333 (6041), 413–414.
Walzer, U., Hendel, R., 2008. Mantle convection and evolution with growing continents. Journal of Geophysical Research 113, B09405.
Walzer, U., Hendel, R., 2009. Predictability of Rayleigh-number and continental–growth evolution of a dynamic model of the Earth's mantle. In: Wagner, S., Steinmetz, M., Bode, A., Brehm, M. (Eds.), High Performance Computing in Science and Engineering '07. Springer, Berlin, pp. 585–600.
Walzer, U., Hendel, R., 2013. Real episodic growth of continental crust or artifact of preservation? A 3-D geodynamic model. Journal of Geophysical Research 118, 2356–2370.
Walzer, U., Hendel, R., Baumgardner, J., 2004. The effects of a variation of the radial viscosity profile on mantle evolution. Tectonophysics 384, 55–90.
Walzer, U., Hendel, R., Köstler, C., Müller, M., Kley, J., Viereck-Götte, L., 2013. A forward model of mantle convection with evolving continents and a model of the Andean subduction orogen. In: Nagel, W.E., Kröner, D.H., Resch, M.M. (Eds.), High Performance Computing in Science and Engineering '12. Springer, Berlin Heidelberg, pp. 473–501.
Wedepohl, K.H., 1995. The composition of the continental crust. Geochimica et Cosmochimica Acta 59, 1217–1232.
White, W.M., 2015. Probing the Earth's deep interior through geochemistry. Geochemical Perspectives 4, 95–246.
White, W.M., Klein, E.M., 2013. The composition of the oceanic crust. In: Rudnick, R.L. (Ed.), The Crust. Treatise on Geochemistry, vol. 3, Elsevier Scientific Publishing Company, Amsterdam, pp. 457–496.
Willbold, M., Stracke, A., 2006. Trace element composition of mantle end-members: implications for recycling of oceanic and upper and lower continental crust. Geochemistry, Geophysics Geosystems 7, Q04004.
Workman, R.K., Hart, S.R., 2005. Major and trace element composition of the depleted MORB mantle (DMM). Earth and Planetary Science Letters 231 (1), 53–72.
Yamazaki, D., Karato, S.I., 2001. Some mineral physics constraints on the rheology and geothermal structure of the Earth's lower mantle. American Mineralogist 86, 385–391.
Yin, Q.Z., Wimpenny, J., Tollstrup, D., Mange, M., Dewey, J., Zhou, Q., Li, X.H., Wu, F.Y., Li, Q.L., Liu, Y., et al. 2012. Crustal evolution of the South Mayo Trough, western Ireland, based on U-Pb ages and Hf-O isotopes in detrital zircons. Journal of the Geological Society 169 (6), 681–689.
Yoneda, A., Osako, M., Ito, E., 2009. Heat capacity measurement under high pressure: a finite element method assessment. Physics of the Earth and Planetary Interiors 174, 309–314.
Yoshida, M., 2012. Dynamic role of the rheological contrast between cratonic and oceanic lithospheres in the longevity of cratonic lithosphere: a three-dimensional numerical study. Tectonophysics 532-535, 156–166.
Yoshida, M., Santosh, M., 2011. Supercontinents, mantle dynamics and plate tectonics: a perspective based on conceptual vs. numerical models. Earth Science Reviews 105 (1), 1–24.